Configurational fingerprints of multicellular living systems

Haiqian Yang[a], Adrian F. Pegoraro[b], Yulong Han[a], Wenhui Tang[a], Rohan Abeyaratne[a], Dapeng Bi[c], and Ming Guo[a,1]

[a]Department of Mechanical Engineering, Massachusetts Institute of Technology, Cambridge, MA 02139; [b]Department of Physics, University of Ottawa, Ottawa, ON K1N 6N5, Canada; and [c]Department of Physics, Northeastern University, Boston, MA 02115

Edited by Sulin Zhang, Pennsylvania State University, University Park, PA, and accepted by Editorial Board Member John A. Rogers September 14, 2021 (received for review May 17, 2021)

Cells cooperate as groups to achieve structure and function at the tissue level, during which specific material characteristics emerge. Analogous to phase transitions in classical physics, transformations in the material characteristics of multicellular assemblies are essential for a variety of vital processes including morphogenesis, wound healing, and cancer. In this work, we develop configurational fingerprints of particulate and multicellular assemblies and extract volumetric and shear order parameters based on this fingerprint to quantify the system disorder. Theoretically, these two parameters form a complete and unique pair of signatures for the structural disorder of a multicellular system. The evolution of these two order parameters offers a robust and experimentally accessible way to map the phase transitions in expanding cell monolayers and during embryogenesis and invasion of epithelial spheroids.

phase transition | jamming | order parameter | cell mechanics | multicellular system

Cells interact and cooperate at length scales far above individuals (1, 2); these long-ranged interactions help determine tissue-level material characteristics. The ability to tune these material characteristics is important for many multicellular physiological and pathological processes including embryogenesis (3–5), cancer invasion (6, 7), and wound healing (8). In these vital processes in living systems (9–11), cells bear many of the hallmarks of a material phase transition (12). In wound healing, for example, cells near the wound edge appear to undergo a solid-to-fluid transition, becoming highly migratory, leading the wound closure (8). Another example is tumor metastasis: benign tumors can maintain a stable configuration for decades; in contrast, cancers might spread all over the body in a short time. In this sense, benign tumors are as rigid as solids, while cancers are rather amorphous like fluids and cells that escape the tumor mass behave more like a gas.

It remains elusive what order parameters are suitable to describe phase transitions in multicellular systems (13). Efforts have been made mainly based on quantifying cell motion such as effective diffusivity, aligning and swirling patterns, or morphological parameters such as shape index and aspect ratio (10, 11, 14–28). These are in contrast to classical condensed matter theory in which material rigidity is a direct consequence of spatial order establishment among neighboring particles, a concept has not previously been explored in living systems.

In solid mechanics, classical constitutive material relations are defined in terms of volumetric and shear deformations, which describe the change in structure among neighboring material points (29). Thus, defining such deformations in cellular systems may allow us to establish more general order parameters for multicellular assemblies that are more directly related to classical material properties. Here, we show that volumetric and shear deformations can be defined for amorphous systems and changes in these order parameters are reflective of phase transitions in both particulate and cellular systems. These order parameters are defined solely based on static images and do not rely on dynamic measurements. Using this framework, we characterize the changes that occur during a variety of order–disorder transitions in two dimensions (2D) and three dimensions (3D), including jamming transition of thermal systems and simulated confluent cell monolayers, maturation of a 2D cell monolayer, extending *Drosophila* germband epithelium, and human epithelial spheroids in 3D.

In thermal systems, the energy competition between isotropic (volumetric) and isochoric (shear) deformation identifies three distinct phases (i.e., gas, liquid, and solid). Gas can barely resist volumetric or shear deformation while solid resists both. In between, liquid is often considered as resistant only to volumetric deformation. Theoretically, the isotropic and isochoric invariants of deformation are a pair of mutually independent and complete variables that can fully quantify the local deformation. Here, we demonstrate how to calculate these for a 2D system; this can be extended to 3D as well (details in *SI Appendix*). In 2D, three noncolinear adjacent cells form a triangle. Assuming N triangles can be formed by linking adjacent cells, the nth triangle ($n = 1, 2, \ldots, N$) in current configuration can be expressed as a matrix $\boldsymbol{T}_n = \begin{bmatrix} X_{n1} - X_{n0} & X_{n2} - X_{n0} \\ Y_{n1} - Y_{n0} & Y_{n2} - Y_{n0} \end{bmatrix}$ (Fig. 1*A*), where X_{nm} and Y_{nm} ($m = 0, 1, 2$) are Cartesian coordinates of the mth vertice of the nth triangle. This segmentation

Significance

Tissues are composed of many cells that coordinate in space, through which tissue-level material characteristics emerge. While recent progress revealed that many biological processes are analogous to material phase transitions, a systematic framework to describe the spatial order of complex living systems has been missing, which limits our understanding of material phase transitions in living systems. We develop a unified method to quantify the evolution of spatial order across different types of disordered systems, including jammed thermal systems, two-dimensional cell monolayers, three-dimensional epithelial spheroids, and *Drosophila* embryos. Using scaling analysis, we show successful differentiation of gas-like, liquid-like, and solid-like phases in various living systems.

Author contributions: H.Y. and M.G. designed research; H.Y. performed research; H.Y., A.F.P., Y.H., W.T., R.A., and D.B. contributed new reagents/analytic tools; H.Y. analyzed data; and H.Y., A.F.P., and M.G. wrote the paper.

The authors declare no competing interest.

This article is a PNAS Direct Submission. S.Z. is a guest editor invited by the Editorial Board.

Published under the PNAS license.

[1]To whom correspondence may be addressed. Email: guom@mit.edu.

This article contains supporting information online at http://www.pnas.org/lookup/suppl/doi:10.1073/pnas.2109168118/-/DCSupplemental.

Published October 29, 2021.

Downloaded at Palestinian Territory, occupied on December 1, 2021

www.manaraa.com

method is known as Delaunay triangulation and has been previously used to measure strain for granular materials (30) and during biological tissue development (31, 32). Here, rather than measuring the temporal evolution of strain field, we seek to quantify the degree of disorder of the system at one point in time by comparing to an ideal reference frame. We consider the refence shape to be the simplest shape which can tesselate all space, namely, an equilateral triangle with $\boldsymbol{T}_r = \sqrt{A}\begin{bmatrix} 1 & \frac{1}{2} \\ 0 & \frac{\sqrt{3}}{2} \end{bmatrix}$ (Fig. 1*A*), where $\frac{\sqrt{3}}{4}A$ is the average area of all Delaunay triangles. The corresponding deformation gradient is $\boldsymbol{F}_n = \boldsymbol{T}_n \boldsymbol{T}_r^{-1}$. A pair of independent and complete invariants of the deformation gradient are $vol_n = \det(\boldsymbol{F})$ and $shear_n = \frac{\mathrm{tr}(\boldsymbol{F}^{\mathrm{T}}\boldsymbol{F})}{\det(\boldsymbol{F})} - 2$ (Fig. 1*B*), which reflect how much area each triangle deviates from the average area and how much distortion each triangle has compared to the equilateral ones, respectively. It can be proved that the two deformations are independent of orientation of the reference triangle (Lemma 1 in *SI Appendix*). Tiling up a surface with equilateral triangles results in hexagonal packing, which is found to be the most frequent cell packing in simple epithelia (33). Let λ_i ($i = 1, 2$) be principal stretches. It can be proved that any deformation gradient $\boldsymbol{F}$ can be factored as $\boldsymbol{F} = \boldsymbol{F}_v\boldsymbol{F}_s$, where $\boldsymbol{F}_v$ is a volumetric deformation with equivalent amount of stretch $v = (\lambda_1\lambda_2)^{1/2}$ and $\boldsymbol{F}_s$ is a simple shear with equivalent amount of shear $k = \sqrt{\frac{\lambda_1}{\lambda_2}} - \sqrt{\frac{\lambda_2}{\lambda_1}}$; moreover, vol_n and $shear_n$ represent the real volumetric and shear deformations of each triangle by $vol_n = v^2$ and $shear_n = k^2$ (Lemma 2 in the *SI Appendix*). If we plot ln(*vol*) and ln(*shear*) of all triangles within a system, it generates a unique configurational fingerprint (Figs. 1*C*). Both vol_n and $shear_n$ have logarithmic distributions (Fig. 1*C*). Two characteristics can be identified from the configurational fingerprints: one is the horizontal width of the fingerprint that reflects the degree of density variation across the whole sample, and the other is the mean vertical position of the fingerprint that reflects how regular these triangles are. To quantify the density variation, we define the volumetric order parameter as $\Phi_{vol} = \langle[ln(vol_n)]^2\rangle$; to quantify the average degree of amorphousness, we define the shear order parameter as $\Phi_{shear} = \langle \ln(shear_n)\rangle$, where <> is the ensemble average of all triangles.

To examine these two order parameters in classical thermal systems, we study the jamming transition of amorphous materials in simulation of 2D binary mixtures with harmonic repulsive potentials (34, 35). We simulate three systems with different binary size ratios and increase particle density to reach jamming. As we calculate the volumetric and shear deformations, we find that both types of deformation remain nonzero and highly heterogeneous even at very high densities (Fig. 2*A*). Examining the order parameters, we see at low particle densities a large Φ_{vol} that reflects significant density fluctuations, indicating that the system is compressible, which is a distinctive characteristic of gas. With increasing density, we find that Φ_{vol} eventually stabilizes at a finite value above zero even as particle density increases further (Fig. 2*B*), which is reminiscent of a relatively incompressible amorphous condensed phase. Further increasing density above the first transition point at which Φ_{vol} stabilizes, Φ_{shear} continuously decreases, indicating that the system becomes more ordered in packing but maintains a constant density fluctuation, which are characteristics of a liquid. With even higher density, a second transition point occurs with a sudden decrease of Φ_{shear}. This sudden change in packing order indicates that the system is jammed and becomes solid-like. Indeed, the diverging Φ_{shear} might be related to the diverging viscosity at jamming (12, 36–38). Moreover, jamming is classically defined as systems showing a finite pressure. Interestingly, we find that while Φ_{vol} remains roughly unchanged (Fig. 2*D*), Φ_{shear} scales with pressure (Fig. 2*E*). This result suggests that the rigidity transition in this system is characterized by regulation in packing disorder, Φ_{shear}. Furthermore, this constitutive relationship between Φ_{shear} and pressure should allow the stress at particle interfaces to be calculated by the measured deformations. If this approach was applied to cellular systems, it would be reminiscent of previous work that has shown that relative values of cell–cell tensions can be inferred from static images of confluent cell monolayer by assuming a foam-like structure (39).

To benchmark this framework in confluent living systems, as opposed to particulate systems, we first investigate the jamming process of a self-propelled Voronoi (SPV) model system of confluent cells at different preferred cell perimeter P_0 and self-propelling velocity v_0 (Fig. 3, details in *SI Appendix*), following the methods described previously (27). Compared to the jammed state, the unjammed state has a highly heterogeneous spatial distribution of *vol* and *shear*, which is consistent with

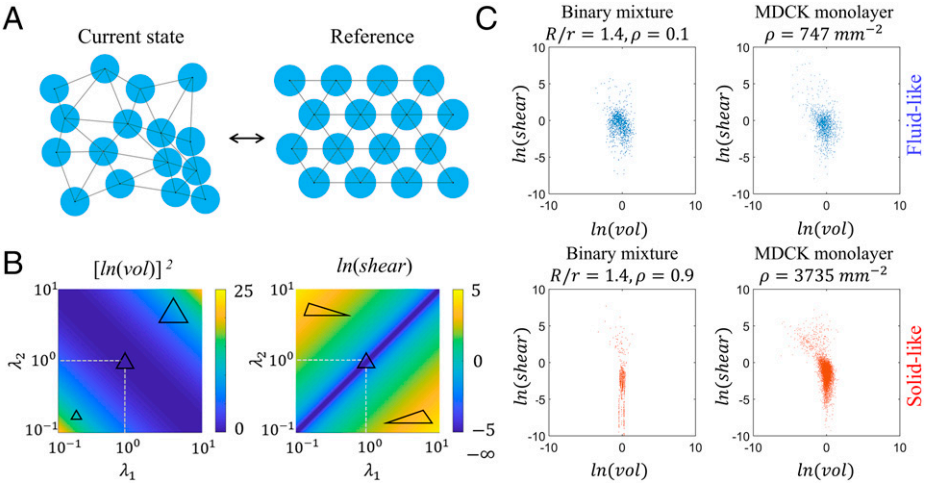

Fig. 1. Schematics and configurational fingerprints. (*A*) Schematics: by comparing particle or cell positions with the reference state of equilateral triangles, the *vol-shear* configurational fingerprints can be calculated. (*B*) $[ln(vol)]^2$ and *ln*(*shear*) with respect to two eigenvalues of deformation gradient λ_1 and λ_2 are symmetric. (*C*) Configurational fingerprints of fluid-like systems are scattered, while those of solid-like systems are compacted.

Downloaded at Palestinian Territory, occupied on December 1, 2021
www.manaraa.com

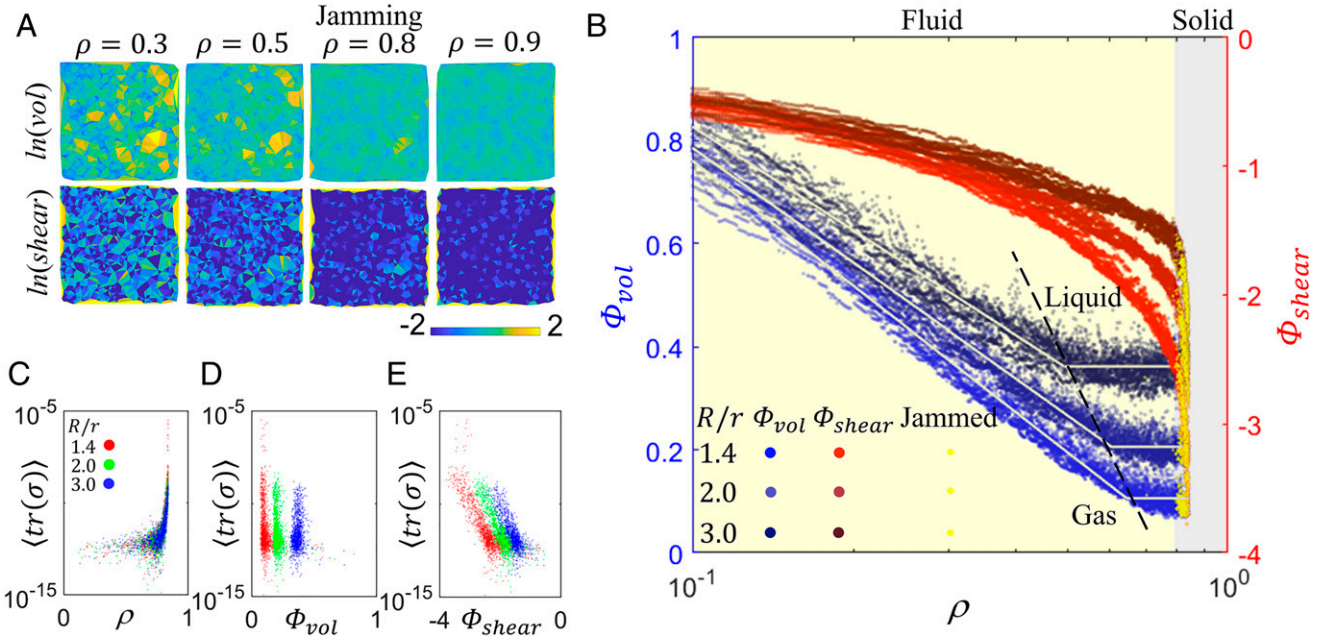

Fig. 2. Φ_{vol} and Φ_{shear} can identify jamming transition in binary mixtures with harmonic potential. (*A*) Spatial distribution of *vol* and *shear* shows that the system maintains amorphous configuration after jamming; (*B*) Φ_{vol} and Φ_{shear} as functions of density. Φ_{vol} converges to different nonzero values at different critical densities, determined by radius ratio; Φ_{shear} suddenly drops at a density around 0.8, exactly at which a finite stress starts to show in these systems, indicating a jammed status. Simulations are performed with a density increment of 0.001, varying from 0.100 to 0.840, and 10 different random initial particle positions. (*C*) Pressure as a function of density. Upon jamming, pressure suddenly grows with increasing density. For R/r = 1.4, 2.0, and 3.0, pressure starts to scale with density after density increases to ~0.8 and stress is ~10^{-11}, so in this system, the classical definition yields 10^{-11} as a threshold for pressure, above which the system is undergoing jamming transition, until it is finally jammed. (*D* and *E*) For systems showing a finite pressure, Φ_{vol} is nearly constant (*D*), and pressure scales with Φ_{shear} (*E*).

shape index (*SI*) (Fig. 3*A*). Using our framework, a sharp transition in Φ_{shear} is observed as the system evolves (Yellow boundary, $\Phi_{shear} = -2$, Fig. 3*B*), which is consistent with the phase boundary given by the median value of shape index ($\bar{SI}$) (Red boundary, $\bar{SI} = 3.813$, Fig. 3*B*). Because this simulated system is fully confluent with constant cell number, although Φ_{vol} slowly increases with increasing P_0 or ν_0, no sharp transition is observed throughout the simulation.

We then analyze confluent multicellular systems from a 2D case with a clear macroscopic pattern, the ventral furrow formation during morphogenesis of *Drosophila* germband epithelium (Fig. 4). The ventral furrow formation is known to be

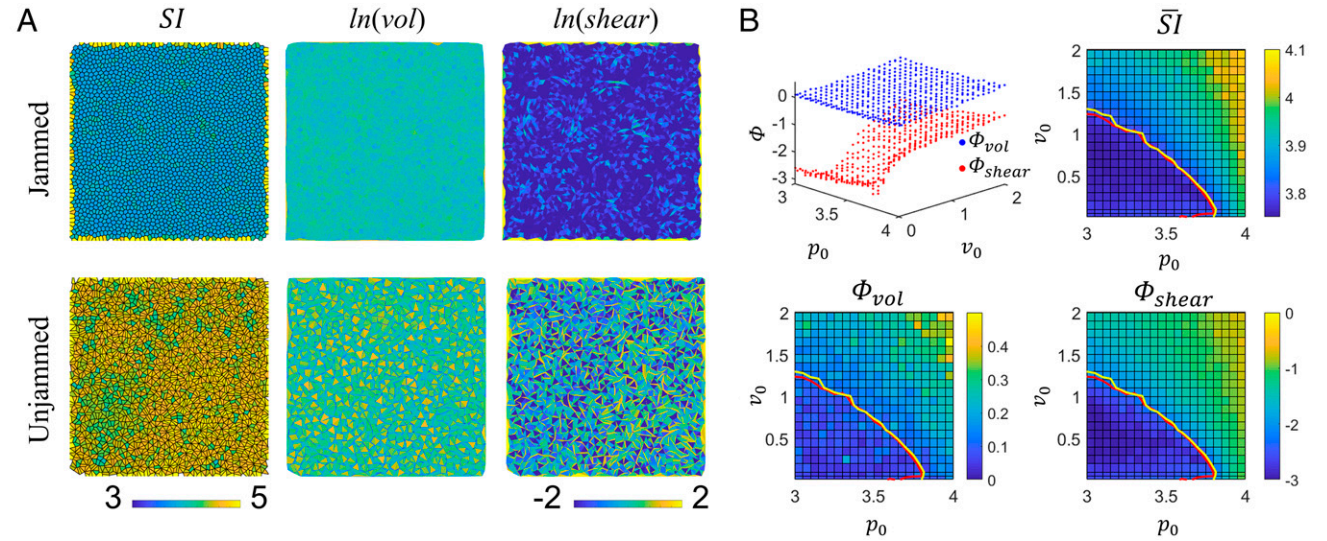

Fig. 3. Φ_{shear} alone marks the jamming transition in SPV model of confluent cell monolayers, while any large change in Φ_{vol} is prohibited due to confluency. (*A*) Spatial distribution of *SI*, ln(*vol*), ln(*shear*) of a jammed (P_0 = 3.000, ν_0 = 0), and an unjammed system (P_0 = 4.591, ν_0 = 0). (*B*) Phase diagram of Φ_{vol}, Φ_{shear}, and $\bar{SI}$ as functions of P_0 and ν_0. Red boundary: $SI = 3.813$, indicating where jamming occurs in this system; yellow boundary: $\Phi_{shear} = -2$. $\bar{SI}$ represents the median value of shape index, and *SI* represents shape index here, which is defined as $SI = P/\sqrt{A}$ where *P* is the perimeter and *A* is the area of each cell. A regular hexagon has an *SI* ~3.72 while a regular pentagon has an *SI* ~3.81, and it was previously shown that a hexagon dominated tissue is solid-like, while fluidization is observed when $\bar{SI}$ ~ 3.81 (10).

Downloaded at Palestinian Territory, occupied on December 1, 2021

www.manaraa.com

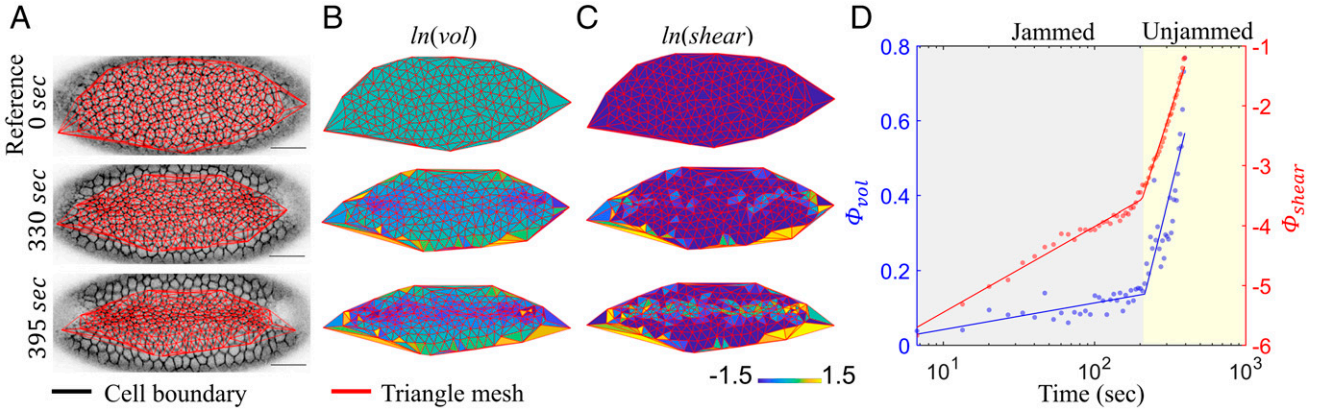

Fig. 4. Two distinct scaling regimes of Φ_{vol} and Φ_{shear} as functions of time during embryogenesis. (*A*) Fluorescent images of the tissue configuration. The reference state is set to be the initial frame. Data are taken from Supplementary Materials of ref. 4. The triangulation mesh is generated by connecting centroid position of cells. (Scale bar, 25 μm.) (*B* and *C*) Low-*vol* (*B*) and high-*shear* (*C*) regions gradually appear. (*D*) Abrupt changes in the scaling law of both order parameters are observed at time ∼200 s.

accompanied by elongation of individual cells in the central region, as can be measured from cell aspect ratios (4). Elongated individual cells, however, do not necessarily lead to changes in spatial order of cells as a collective. Here, we report that this process displays a clear pattern of changes in relative spatial relation among neighboring cells that the central region is not only shearing but also shrinking (Fig. 4 *B* and *C*). More interestingly, both power-law relationships of Φ_{shear} and Φ_{vol} as functions of time are abruptly changed at ∼200 s, as the ventral furrow forms and cell number density changes. The evolution in Φ_{shear} and Φ_{vol} includes two successive but distinct phases: in the first phase, both Φ_{shear} and Φ_{vol} change slowly and the system behaves like jammed, while in the second phase, both Φ_{shear} and Φ_{vol} change rapidly, indicating that the system undergoes unjamming transition.

While confluent cellular systems widely exist, there are many multicellular systems that are nonconfluent, which can also be critical in various physiological and pathological processes; for example, in cancer metastasis, individual cells can escape from the tumor mass. The transition from nonconfluency to confluency might, although not necessarily, lead to a transition in density fluctuation, which is a widely used signature of liquid–gas transition in classical systems (40, 41). Here, we show that in addition to the liquid–solid jamming transition in confluent systems detected by Φ_{shear}, Φ_{vol} further captures this transition of density fluctuation in living systems and defines two distinct phases reminiscent of gas and liquid.

We apply this method to the process of sparsely distributed epithelial cells on 2D forming a confluent monolayer. Previous studies have shown that fluid–solid phase transitions exist in 2D monolayers, as quantified by individual cell dynamics (9), cell shape index (10), and aspect ratio (4). Yet, as sparsely migrating cells behave reminiscent of a gas phase, it has not been distinguished from liquid phase in 2D multicellular systems, possibly due to the lack of proper order parameters that can consistently describe multicellular systems below confluency. Here, we show that this gap can be filled by Φ_{vol}; Φ_{vol} and Φ_{shear} together capture the full picture of the transformation from gas to liquid and finally to amorphous solid of a growing epithelial monolayer. To do so, we culture Madin–Darby Canine Kidney (MDCK) cells on a 2D glass substrate coated with collagen I, allowing them to divide and increase in density. Cells are initially seeded at a very dispersed state, and they gradually reach confluency and approach jamming as density increases (Fig. 5 *A*, *Top*). We image this entire process every 3 min using confocal microscopy. Cells are transfected with green fluorescent protein tagged nuclear localization signal (GFP-NLS) that allows us to see individual nuclei, which we use to calculate the volumetric and shear order parameters of the system. Initially, comparably large Φ_{vol} and Φ_{shear} show significant density fluctuations as well as random arrangement among cells, suggesting a gas-like state. Then the volumetric and shear deformations are simultaneously and gradually restricted following a power-law relation until Φ_{vol} first reaches its inflection point (Fig. 5*B*). This inflection point occurs when the monolayer reaches confluency, with a density around 1,500 mm^{-2}, at which density fluctuation is stabilized, indicating that the cells behave like a relatively incompressible but amorphous liquid. Beyond this point, Φ_{vol} becomes comparably stable, and Φ_{shear} continues to decrease, suggesting that further decrease in the volumetric fluctuation is significantly hindered, but packing disorder is still reduced with increasing density, which is reminiscent of liquid-to-solid transition, consistent with our simulation of confluent monolayers (Fig. 3). Interestingly, unlike the behaviors of binary mixtures in which the stabilized Φ_{vol} is almost unchanged after the first transition point (Fig. 2), a small decrease can still be observed in the volume fluctuation Φ_{vol} of a cell monolayer (Fig. 5*B*), although changing at a comparably slower rate compared to the gas state. This is similar to the jammed phase of the embryo (Fig. 4), in which the cells start to slowly deform. The rate of changes in Φ_{vol} in the jammed state thus may reflect deformability of the monolayer. The second inflection point is identified by Φ_{shear}, which marks the endpoint of the fluid phase, at a density ∼2,600 mm^{-2}, after which both Φ_{vol} and Φ_{shear} do not further decrease, indicating a jammed state; this critical density is consistent with previous report in MDCK monolayer (∼2,800 mm^{-2}) identified based on significantly reduced cell speed and increased pack size (9).

Furthermore, results in the gas–liquid transition regime also reveal that these adhesive epithelial cells develop spatial order long before they are connected into a complete monolayer. Indeed, below confluency, rather than evenly distributed, cells form packs with void regions among these packs, as can be seen from the microscopic images (Fig. 5 *A*, *Top*). This is analogous to nucleation of sparse adhesive particles whose potential energy is dominating over kinetic energy (*SI Appendix*, Fig. S1 *A–C*); with higher density, these packs aggregate into larger ones (*SI Appendix*, Fig. S1 *D–F*). Interestingly, while cells in the packs are more elongated and polarized below confluency, their shapes gradually become more isotropic with increasing density. Moreover, similar to the binary mixture, the stabilized Φ_{vol} is nonzero, suggesting an intrinsic disorder in the monolayer. Since the

Downloaded at Palestinian Territory, occupied on December 1, 2021
www.manaraa.com

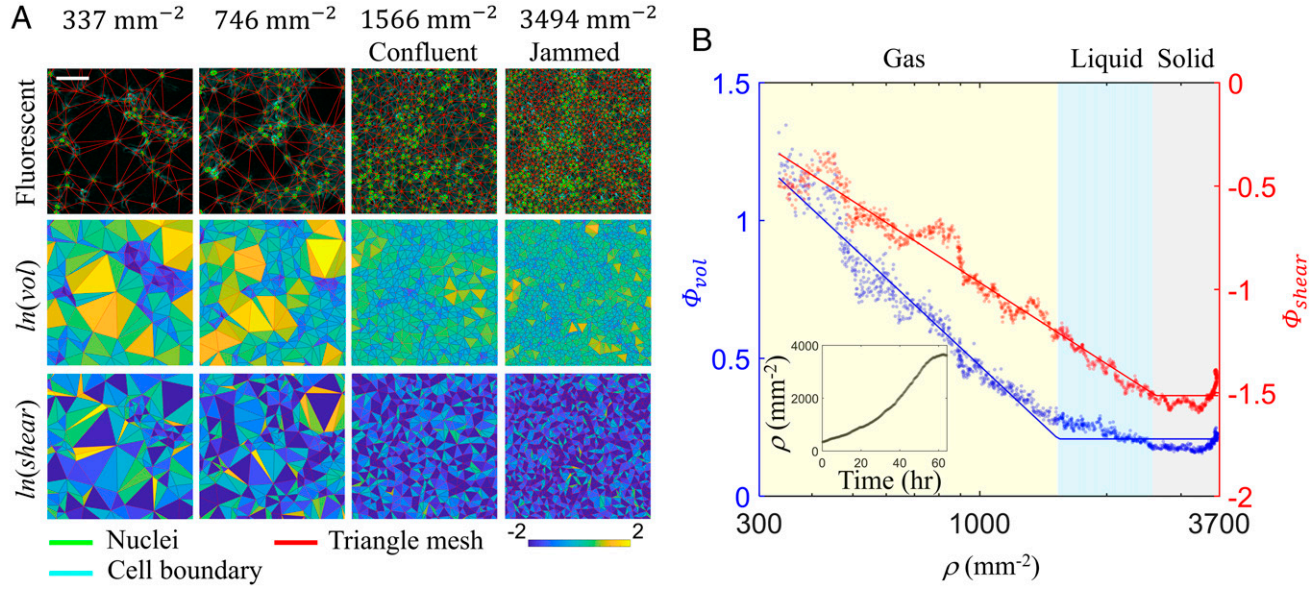

Fig. 5. Φ_{vol} and Φ_{shear} identify three scaling regimes against increasing density (i.e., gas-like, liquid-like, and solid-like states of epithelial cell monolayer). (*A*) Heterogeneity in both *vol* and *shear* decays with increasing cell density. (Scale bar, 100 μm.) (*B*) With increasing cell density, both Φ_{vol} and Φ_{shear} first decrease following power-law relations, at which stage comparably large Φ_{vol} and Φ_{shear} suggest that the system is reminiscent of a gas. The first critical transition point is indicated by the power-law slope change in Φ_{vol}, after which density fluctuations are constrained, while Φ_{shear} may still decrease following the same power law, indicating that the system is amorphous but incompressible and, thus, is reminiscent of a liquid; the second critical transition point is then reached indicated by the power-law slope change in Φ_{shear}, after which packing disorder is regulated at a finite value, which is analogous to an amorphous solid. (*Inset*) Cell density increases with time.

monolayer is already confluent at this stage, this is possibly resulted from volume fluctuation of individual cells. Besides the natural difference among individuals, this may be due to cell division or asynchronous swelling and shrinking during cell cycle. For different systems, perturbing the degree of this volume heterogeneity may also influence the critical transition points. As a minimal model, the binary systems of different binary ratio have different level of size fluctuations, and systems with larger size fluctuations exhibit a shift of the first transition point to lower density (Fig. 2*B*). The spatial distributions of local volumetric and shear deformations show that the system gradually becomes more homogeneous as the monolayer approaches jamming (Fig. 5*A*). Additionally, the evolution of the two order parameters in the liquid–solid transition regime suggests that it is not restrictions on volumetric deformation but rather on shear deformation that drives this liquid-to-solid transition. This is consistent with previous results predicting density-independent transitions in cell monolayers at critical cell-shape parameters (4, 10); the reduced shear deformation indicates more isotropic shape of each cell, which corresponds to reduced cell aspect ratio and shape index in confluent systems. To further test this intuition, we perform measurements on cells that have undergone epithelial-to-mesenchymal transition (EMT) and find that restrictions in volumetric deformations still occur, suggesting a gas–liquid transition can occur, whereas restrictions in shear deformation are ablated, suggesting jamming does not occur (*SI Appendix*, Fig. S2). Such a result is consistent with recent findings that EMT and jamming/unjamming offer distinct pathways to collective cellular motion (42).

While 2D cell monolayers such as epithelia widely exist in nature, cells are mostly organized in a 3D space in tissues and organs. To examine whether volumetric and shear order parameters can also describe changes in material characteristics in 3D multicellular systems, we investigate the invasion process of epithelial spheroids in 3D. To do so, we grow human mammary epithelial spheroids from MCF-10A cells in an interpenetrating gel containing 5 mg/mL alginate and 4 mg/mL Matrigel. These cells form a spheroid shape in the first several days after seeding (Fig. 6 *A*, *Top*) and become invasive and migrate into the surrounding matrix in about 7 to 10 d (Fig. 6 *A*, *Bottom*); this system has been previously used to model tumor invasion (43–45). To visualize individual cell nuclei, we transfect these cells to express GFP-NLS. Using these nuclear positions, we calculate volumetric and shear order parameters in 3D (details in *SI Appendix*). Interestingly, comparing to noninvasive spheroids (day 5), we find that invasive spheroids (day 10) have no significant difference in Φ_{shear} but much larger Φ_{vol} (Fig. 6*D*); both order parameters are far from the baseline values of a face-centered cubic crystal. This indicates that while both invasive and noninvasive spheroids are highly amorphous, there is no significant difference in the degree of amorphousness, but the invasive spheroids have a much larger density variation. If making an analogy with classical thermal phases, in which the solid–liquid transition is mainly due to changes in amorphousness, and the liquid–gas transition is mainly due to changes in density variation, the transition from noninvasive spheroids to invasive ones are not only analogous to fluidization but more specifically from liquid-like to gas-like. Furthermore, comparing to the core of the spheroid, we find that cells in the protrusion have larger *shear* but not obviously different *vol* (Fig. 6 *B* and *C*), suggesting that the invasive protrusions are more distorted compared to the core. The branch having a larger *shear* is consistent with the spatial distribution of cell trajectories in which we find that cells move collectively toward the invasive protrusion (Fig. 6 *A*, *Bottom*). This suggests that cells need to deform and squeeze as a collective group to invade into the surrounding matrix. This partially validates the previous hypothesis that confinement of the matrix is a key resistance that migratory cells confront to break away from the original cluster (7, 46) and the fact that leader cells in collective migration often have a more elongated mesenchymal shape (6). Interestingly, as we perform immunofluorescent imaging of vimentin, a type of intermediate filament that is up-regulated during EMT, we find that vimentin is indeed up-regulated in the invasive branches

Downloaded at Palestinian Territory, occupied on December 1, 2021

www.manaraa.com

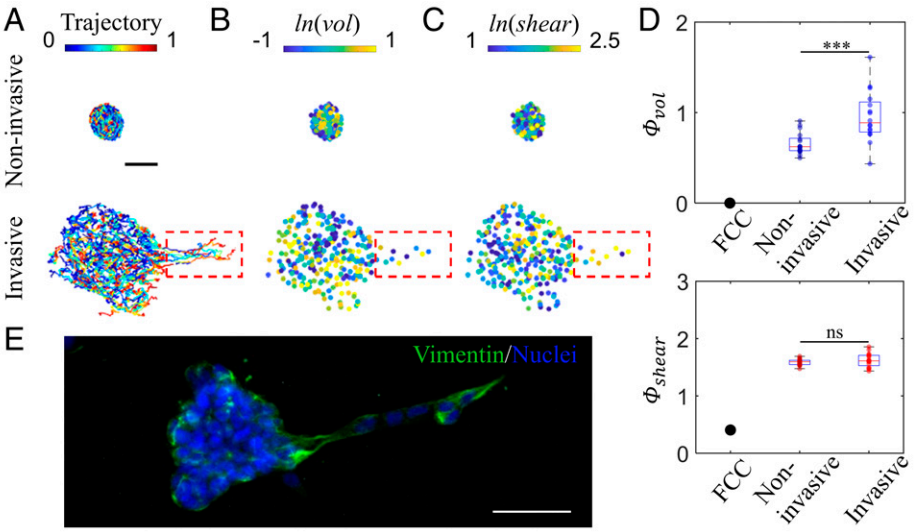

Fig. 6. Invasive epithelial spheroids have larger density variations but no significant difference in amorphousness. (*A*) Typical cell trajectories. (*B* and *C*) Typical spatial distribution of *vol* (*B*) and *shear* (*C*). Dash box: the protrusion has more dynamic cells and larger shear deformation but similar volumetric deformation compared to the core. (Scale bar, 50 μm.) (*D*) Φ_{vol} and Φ_{shear} of noninvasive ($n = 17$) and invasive spheroids ($n = 16$). While volumetric order is significantly higher for invasive spheroids, shear order for both invasive and noninvasive spheroids are similarly large. Both order parameters deviate far from face-centered cubic crystalline structure. Student's *t* test is used to evaluate statistical difference. ***: $P < 0.001$; ns: no significant difference. FCC: face-centered cubic crystal structure. (*E*) Fluorescent imaging of vimentin intermediate filaments and nuclei. (Scale bar, 50 μm.)

(Fig. 6*E*). Thus, a possible explanation for invasive spheroids becoming more disordered is that loss of intercellular adhesion as a result of EMT may lead to unjamming of a cellular collective (13). To summarize, the spatial and temporal changes of volumetric and shear orders suggest that invasive mammary epithelial spheroids can tune their material properties to colonize new territories and remodel their configuration.

In conclusion, we define two order parameters, volumetric order (Φ_{vol}) and shear order (Φ_{shear}), to quantify the structure among neighboring cells in multicellular living systems. Φ_{vol} and Φ_{shear} form a complete description of structural order: Φ_{vol} describes the degree of density disorder, which reflects factors such as nonconfluency (Figs. 2, 5, and 6) and size/density heterogeneity (Figs. 2, 4, and 5), while Φ_{shear} characterizes packing disorder resulting from factors such as jamming transition (Figs. 2–5) and anisotropic cell shapes (Figs. 4–6). We first show that Φ_{vol} and Φ_{shear} can describe phase transitions in particulate systems. Interestingly, once jamming is initiated, Φ_{shear} scales with internal pressure (Fig. 2*E*), which suggests a potential noninvasive measurement of stress from only static images. Then, we demonstrate that Φ_{shear} alone is equivalent to shape index in determining the jamming phase boundary in an SPV simulation of confluent cell monolayer. Moreover, we identify two scaling regimes during *Drosophila* embryogenesis and show that previously observed elongation of individual cells is resulted from not only changes in packing but also changes in volume of the space among neighboring cells (Fig. 4). We further show the importance of Φ_{vol} in studying those nonconfluent living systems. Applying this framework to a growing epithelial monolayer reveals a gas-like state of monolayers below confluency, a liquid-like state upon monolayer maturation, and then a solid-like state when the monolayer is jammed (Fig. 5). Interestingly, we also find that induction of EMT changes the power-law scaling in both Φ_{vol} and Φ_{shear} as functions of cell density (*SI Appendix*, Fig. S2). Finally, with this framework, we find that invasive 3D human mammary epithelial spheroids have significantly larger density variation Φ_{vol} but no significant difference in the degree of amorphousness Φ_{shear} compared to their noninvasive counterparts; moreover, particularly high shear deformation is observed in the invasive branches (Fig. 6).

An intriguing question in cell mechanobiology is how tissue-level order emerges within a group of cells. It is known that it starts from single-cell scale, regulated by genetics and cell signaling, and manifests at the tissue and organ scale setting tissue morphology, rigidity, function, etc. However, a structural description between the two length scales remains elusive; indeed, while local interaction of a cell with its close neighbors plays a critical role in regulating material characteristics of tissues, it has been difficult to characterize this interaction, particularly in situ. Thus, the framework and two order parameters introduced here may reveal important structural information that was not previously accessible during processes such as wound healing and cancer metastasis. Furthermore, this methodology could be used to monitor how structural characteristics are influenced by mechanical or biochemical perturbations.

We expect that this method may provide a morphological assay for histopathology evaluation. In traditional histopathology, individual cell morphology and tissue structure are two main features typically being examined. Breast cancer grade, for example, is determined based on nuclear pleomorphism, cell division, and gland or tubule formation (47). However, there is growing evidence from in vitro experiments showing that intercellular interactions such as formation of gap junctions are also important for invasion in epithelial-derived model tumor spheroids (2). Volumetric and shear order parameters reveal clear geometrical information of the local structure among neighboring cells that was missing in previous morphological assays; these order parameters can be readily incorporated into existing diagnostic pipelines and might serve as an additional marker for diagnosis. As this method is solely based on analyzing static images, it can be readily applied to histopathological data with a simple staining method visualizing cell positions, such as biopsy samples with stained cell nuclei. While 2D structures widely exist in nature, objects are often not only located on a 2D plane but instead span in 3D. For 3D structures or samples with substantial out-of-plane deformations, a full 3D reconstruction using methods such as confocal

Downloaded at Palestinian Territory, occupied on December 1, 2021

www.manaraa.com

microscopy or stereography would be necessary. It is worth noting that when we attempt to directly apply the 2D method to a 2D image obtained from a regular monocular optical system, the out-of-plane structure in this scenario can effectively result in artificial shape changes that are not distinguishable from real in-plane changes. Thus, even for a quasi-2D structure, if out-of-plane deformations cannot be ruled out, a full 3D structure should first be constructed, then a projected 2D image can be generated for calculating the 2D order parameters.

The volumetric and shear order parameters essentially quantify the system-specific distances from the current state to the reference state; they increase as the system configuration deviates from the reference state. In the current study, the reference configurations are mostly assumed to be equilateral triangles. Consequently, the configuration having the most congruent and equilateral triangles will have the smallest value of both order parameters. In less-controlled situations, this equilateral configuration may still serve as a reasonable reference, while system configurations within a certain distance to it might not be achievable due to factors such as intrinsic size variation within the population, asynchronous shrinking and swelling of cells, naturally anisotropic tissue, or substrate curvature. In these situations, real configurations can be used as a reference as well and might help with data interpretation (Fig. 4*D* and *SI Appendix*, Fig. S4). Two natural choices are the most ordered and the most disordered real configurations: as the system becomes more disordered, the two parameters increase if using the most ordered real state as the reference (Fig. 4*D*), similar to using equilateral triangles (*SI Appendix*, Fig. S4*A*); they decrease if using the most disordered real state as the reference (*SI Appendix*, Fig. S4*C*). In Fig. 4*D*, the reference state is taken as the initial frame in which no global pattern is distinguishable from the image, which allows *vol* and *shear* to precisely reflect the deformation compared to the initial frame. The reference state can also be set around the critical transition point, and the order parameters would reflect the system-specific distances from the transition point, which may help reveal more details of the system behaviors near the transition point; however, as this specific state has an intermediate level of disorder, both order parameters are nonmonotonic using this reference (*SI Appendix*, Fig. S4*B*). Nevertheless, although using real system configurations as an alternative may provide useful information, the fact that they require a real configuration of each sample to be identified as the reference might introduce challenges to interpreting the data when applying the technique to complex processes. Furthermore, sample-specific reference states make it challenging to compare across different samples. By contrast, using equilateral triangles as reference is simple and general, especially when studying noisy data such as clinical samples. For in vivo applications, the equilateral triangles may always be a first choice; in some cases, if it is desired to know the similarity between a specific configuration and an arbitrary one in terms of volumetric and shear deformations, this specific one can be set as the reference.

The framework we introduce here is general and unified, such that can be applied to systems both on 2D and in 3D and to both confluent and dispersed multicellular systems. Based on cell locations, we can characterize material phases and identify important changes in materials states that may contribute to important biological processes of the tissue. Using this framework, we can resolve details in evolution of material characteristics starting from extremely low density to full confluency and eventually jammed states. The generality and robustness of this framework allow that different systems can be compared in a consistent way.

Materials and Methods

Cell culture, microscopy, and simulation details are described in *SI Appendix*. Briefly, particle or cell positions of different systems were recorded, from which volumetric and shear order parameters were calculated. Binary mixtures with one-sided harmonic potential energy of different particle size ratios and densities were simulated with the fast inertial relaxation engine algorithm (48). SPV simulations of confluent cell monolayers were performed with different preferred cell perimeter P_0 and self-propelling velocity v_0 following the methods in ref. 27. MDCK and MCF-10A cells were transfected with GFP-NLS to visualize nuclear positions. For 2D culture, cells were seeded at low density on collagen-coated glass substrate and allowed to divide until forming a jammed monolayer with a stable density. For 3D spheroid culture, MCF-10A cells were grown in an interpenetrating gel containing 5 mg/mL alginate and 4 mg/mL Matrigel, and nuclear positions were recorded on day 5 and 10 after seeding. Images were recorded on Leica SP5 and SP8 confocal microscopes and nuclear positions were tracked with TrackMate in ImageJ (49).

Data Availability. All study data are included in the article and/or *SI Appendix*.

ACKNOWLEDGMENTS. We would like to acknowledge the support from the NIH (1R01GM140108), the MathWorks, and the Jeptha H. and Emily V. Wade Award at the Massachusetts Institute of Technology. A.F.P. acknowledges the Natural Sciences and Engineering Research Council of Canada (Discovery and Collaborative Research and Development grants to A. Stolow), the National Research Council of Canada–University of Ottawa Joint Centre for Extreme Photonics, and the Max-Planck-University of Ottawa Centre for Extreme and Quantum Photonics. M.G. acknowledges the Sloan Research Fellowship. D.B. acknowledges support from NSF (DMR-2046683).

1. D. T. Tambe *et al.*, Collective cell guidance by cooperative intercellular forces. *Nat. Mater.* **10**, 469–475 (2011).
2. Y. L. Han *et al.*, Cell swelling, softening and invasion in a three-dimensional breast cancer model. *Nat. Phys.* **16**, 101–108 (2019).
3. P. J. Keller, Imaging morphogenesis: Technological advances and biological insights. *Science* **340**, 1234168 (2013).
4. L. Atia *et al.*, Geometric constraints during epithelial jamming. *Nat. Phys.* **14**, 613–620 (2018).
5. A. Mongera *et al.*, A fluid-to-solid jamming transition underlies vertebrate body axis elongation. *Nature* **561**, 401–405 (2018).
6. P. Friedl, D. Gilmour, Collective cell migration in morphogenesis, regeneration and cancer. *Nat. Rev. Mol. Cell Biol.* **10**, 445–457 (2009).
7. O. Ilina *et al.*, Cell-cell adhesion and 3D matrix confinement determine jamming transitions in breast cancer invasion. *Nat. Cell Biol.* **22**, 1103–1115 (2020).
8. A. Brugués *et al.*, Forces driving epithelial wound healing. *Nat. Phys.* **10**, 683–690 (2014).
9. T. E. Angelini *et al.*, Glass-like dynamics of collective cell migration. *Proc. Natl. Acad. Sci. U.S.A.* **108**, 4714–4719 (2011).
10. D. Bi, J. Lopez, J. M. Schwarz, M. L. Manning, A density-independent rigidity transition in biological tissues. *Nat. Phys.* **11**, 1074–1079 (2015).
11. M. Merkel, M. L. Manning, A geometrically controlled rigidity transition in a model for confluent 3D tissues. *New J. Phys.* **20**, 022002 (2018).
12. V. Trappe, V. Prasad, L. Cipelletti, P. N. Segre, D. A. Weitz, Jamming phase diagram for attractive particles. *Nature* **411**, 772–775 (2001).
13. C. A. La Porta, S. Zapperi, Phase transitions in cell migration. *Nat. Rev. Phys.* **2**, 516–517 (2020).
14. X. Trepat, E. Sahai, Mesoscale physical principles of collective cell organization. *Nat. Phys.* **14**, 671–682 (2018).
15. B. Szabó *et al.*, Phase transition in the collective migration of tissue cells: Experiment and model. *Phys. Rev. E Stat. Nonlin. Soft Matter Phys.* **74**, 061908 (2006).
16. T. Vicsek, A. Czirók, E. Ben-Jacob, I. Cohen, O. Shochet, Novel type of phase transition in a system of self-driven particles. *Phys. Rev. Lett.* **75**, 1226–1229 (1995).
17. H. Wang, S. Lacoche, L. Huang, B. Xue, S. K. Muthuswamy, Rotational motion during three-dimensional morphogenesis of mammary epithelial acini relates to laminin matrix assembly. *Proc. Natl. Acad. Sci. U.S.A.* **110**, 163–168 (2013).
18. M. Sadati, N. Taheri Qazvini, R. Krishnan, C. Y. Park, J. J. Fredberg, Collective migration and cell jamming. *Differentiation* **86**, 121–125 (2013).
19. T. D. Yang, H. Kim, C. Yoon, S.-K. Baek, K. J. Lee, Collective pulsatile expansion and swirls in proliferating tumor tissue. *New J. Phys.* **18**, 103032 (2016).
20. T. E. Angelini, E. Hannezo, X. Trepat, J. J. Fredberg, D. A. Weitz, Cell migration driven by cooperative substrate deformation patterns. *Phys. Rev. Lett.* **104**, 168104 (2010).
21. S.-Z. Lin, Y. Li, J. Ji, B. Li, X.-Q. Feng, Collective dynamics of coherent motile cells on curved surfaces. *Soft Matter* **16**, 2941–2952 (2020).
22. X. Wang *et al.*, Anisotropy links cell shapes to tissue flow during convergent extension. *Proc. Natl. Acad. Sci. U.S.A.* **117**, 13541–13551 (2020).
23. G. Erdemci-Tandogan, M. J. Clark, J. D. Amack, M. L. Manning, Tissue flow induces cell shape changes during organogenesis. *Biophys. J.* **115**, 2259–2270 (2018).

Downloaded at Palestinian Territory, occupied on December 1, 2021

www.manaraa.com

24. M. Czajkowski, D. M. Sussman, M. C. Marchetti, M. L. Manning, Glassy dynamics in models of confluent tissue with mitosis and apoptosis. *Soft Matter* **15**, 9133–9149 (2019).
25. P. Sahu *et al.*, Small-scale demixing in confluent biological tissues. *Soft Matter* **16**, 3325–3337 (2020).
26. C. Malinverno *et al.*, Endocytic reawakening of motility in jammed epithelia. *Nat. Mater.* **16**, 587–596 (2017).
27. D. Bi, X. Yang, M. C. Marchetti, M. L. Manning, Motility-driven glass and jamming transitions in biological tissues. *Phys. Rev. X* **6**, 021011 (2016).
28. D. Volfson, S. Cookson, J. Hasty, L. S. Tsimring, Biomechanical ordering of dense cell populations. *Proc. Natl. Acad. Sci. U.S.A.* **105**, 15346–15351 (2008).
29. A. G. Holzapfel, *Nonlinear Solid Mechanics II* (John Wiley & Sons, 2000).
30. K. Bagi, Analysis of microstructural strain tensors for granular assemblies. *Int. J. Solids Struct.* **43**, 3166–3184 (2006).
31. R. Etournay *et al.*, Interplay of cell dynamics and epithelial tension during morphogenesis of the Drosophila pupal wing. *eLife* **4**, e07090 (2015).
32. B. Guirao *et al.*, Unified quantitative characterization of epithelial tissue development. *eLife* **4**, e08519 (2015).
33. M. C. Gibson, A. B. Patel, R. Nagpal, N. Perrimon, The emergence of geometric order in proliferating metazoan epithelia. *Nature* **442**, 1038–1041 (2006).
34. A. J. Liu, S. R. Nagel, The jamming transition and the marginally jammed solid. *Annu. Rev. Condens. Matter Phys.* **1**, 347–369 (2010).
35. C. S. O'Hern, L. E. Silbert, A. J. Liu, S. R. Nagel, Jamming at zero temperature and zero applied stress: The epitome of disorder. *Phys. Rev. E Stat. Nonlin. Soft Matter Phys.* **68**, 011306 (2003).
36. J. C. Mauro, Y. Yue, A. J. Ellison, P. K. Gupta, D. C. Allan, Viscosity of glass-forming liquids. *Proc. Natl. Acad. Sci. U.S.A.* **106**, 19780–19784 (2009).
37. P. Olsson, S. Teitel, Critical scaling of shear viscosity at the jamming transition. *Phys. Rev. Lett.* **99**, 178001 (2007).
38. A. Ikeda, L. Berthier, P. Sollich, Unified study of glass and jamming rheology in soft particle systems. *Phys. Rev. Lett.* **109**, 018301 (2012).
39. R. Vasan, M. M. Maleckar, C. D. Williams, P. Rangamani, DLITE uses cell-cell interface movement to better infer cell-cell tensions. *Biophys. J.* **117**, 1714–1727 (2019).
40. M. Rovere, D. W. Heermann, K. Binder, The gas-liquid transition of the two-dimensional Lennard-Jones fluid. *J. Phys. Condens. Matter* **2**, 7009 (1990).
41. H. Watanabe, N. Ito, C.-K. Hu, Phase diagram and universality of the Lennard-Jones gas-liquid system. *J. Chem. Phys.* **136**, 204102 (2012).
42. J. A. Mitchel *et al.*, In primary airway epithelial cells, the unjamming transition is distinct from the epithelial-to-mesenchymal transition. *Nat. Commun.* **11**, 5053 (2020).
43. O. Chaudhuri *et al.*, Extracellular matrix stiffness and composition jointly regulate the induction of malignant phenotypes in mammary epithelium. *Nat. Mater.* **13**, 970–978 (2014).
44. M. J. Paszek *et al.*, Tensional homeostasis and the malignant phenotype. *Cancer Cell* **8**, 241–254 (2005).
45. K. R. Levental *et al.*, Matrix crosslinking forces tumor progression by enhancing integrin signaling. *Cell* **139**, 891–906 (2009).
46. P. Friedl, K. Wolf, Plasticity of cell migration: A multiscale tuning model. *J. Cell Biol.* **188**, 11–19 (2010).
47. A. E. Giuliano *et al.*, Breast cancer—Major changes in the American Joint Committee on Cancer eighth edition cancer staging manual. *CA Cancer J. Clin.* **67**, 290–303 (2017).
48. E. Bitzek, P. Koskinen, F. Gähler, M. Moseler, P. Gumbsch, Structural relaxation made simple. *Phys. Rev. Lett.* **97**, 170201 (2006).
49. J.-Y. Tinevez *et al.*, TrackMate: An open and extensible platform for single-particle tracking. *Methods* **115**, 80–90 (2017).

Downloaded at Palestinian Territory, occupied on December 1, 2021

www.manaraa.com